Conduction Velocity, G-ratio, and Extracellular Water as Microstructural Characteristics of Autism Spectrum Disorder

Benjamin T. Newman[1,2], Zachary Jacokes[3], Siva Venkadesh[1], Sara J. Webb[4,5], Natalia M. Kleinhans[6], James C. McPartland[7,8], T. Jason Druzgal[2], Kevin A. Pelphrey[2], John Darrell Van Horn[1,3*]

For the GENDAAR Research Consortium

[1]Department of Psychology, University of Virginia, Gilmer Hall, Charlottesville, VA 22903

[2]UVA School of Medicine, University of Virginia, 560 Ray Hunt Drive, Charlottesville, VA 22903

[3]School of Data Science, University of Virginia, Elson Building, Charlottesville, VA 22903

[4]Department of Psychiatry and Behavioral Science, University of Washington, Seattle WA USA 98195

[5]Seattle Children's Research Institute, 1920 Terry Ave, Building Cure-03, Seattle WA 98101

[6]Department of Radiology, Integrated Brain Imaging Center, University of Washington, 1959 NE Pacific St Seattle, WA 98195

[7]Yale Child Study Center, 230 South Frontage Road, New Haven, CT 06520

[8]Yale Center for Brain and Mind Health, 40 Temple Street, Suite 6A, New Haven, CT, 06520

Email: jdv7g@virginia.edu

Words in Abstract: 245

Words in Body: 3,921

Figures: 9

Tables: 1

Running Head: *Neural Conduction Velocities in ASD*

Abstract:

The neuronal differences contributing to the etiology of autism spectrum disorder (ASD) are still not well defined. Previous studies have suggested that myelin and axons are disrupted during development in ASD. By combining structural and diffusion MRI techniques, myelin and axons can be assessed using extracellular water, aggregate g-ratio, and a novel metric termed aggregate conduction velocity, which is related to the capacity of the axon to carry information. In this study, several innovative cellular microstructural methods, as measured from magnetic resonance imaging (MRI), are combined to characterize differences between ASD and typically developing adolescent participants in a large cohort. We first examine the relationship between each metric, including microstructural measurements of axonal and intracellular diffusion and the T1/T2 ratio. We then demonstrate the sensitivity of these metrics by characterizing differences between ASD and neurotypical participants, finding widespread increases in extracellular water in the cortex and decreases in aggregate g-ratio and aggregate conduction velocity throughout the cortex, subcortex, and white matter skeleton. This study is the first to reveal that ASD involves differences of myelin and axonal development with implications for neuronal function. We also introduce a novel neuroimaging metric, aggregate conduction velocity, that is highly sensitive to these changes. We conclude that ASD may be characterized by otherwise intact structural connectivity but that functional connectivity may be attenuated by network properties affecting neural transmission speed. This effect may explain the putative reliance on local connectivity in contrast to more distal connectivity observed in ASD.

Keywords: Conduction velocity; diffusion MRI; autism spectrum disorder; sex differences

Introduction:

Autism spectrum disorder (ASD) represents a complex, multifaceted condition having a significant sex bias in both diagnosis rate and behavioral symptom profile[1]. This sex difference has driven considerable research interest in determining diagnostic and sex-specific associations with brain structure and function as measurable using magnetic resonance imaging (MRI)-based techniques.

ASD Neuroimaging: MRI techniques have long been a focus in ASD for potential diagnosis and increased understanding of brain patterns that might explain symptom severity and clinical variation. Reviews of neuroimaging literature going back as far as 2003 report consistently detectable mean increases in total brain, parietal, temporal, and cerebellar volumes compared to typically developing (TD) comparison subjects, though there were apparent differences in findings depending on the age cohort being studied and an almost total lack of female subjects[2,3]. Using a large subset of male subjects from the Autism Brain Imaging Data Exchange (ABIDE), a more recent study has described widespread increased cortical thickness that diverges from TD during childhood but rapidly decreases to levels equivalent to TD participants upon entering adulthood[4]. Another study supported this finding, used a distance-based feature selection paradigm to find differences within paired ASD/TD subjects to see differences in cortical thickness that may map to areas key to functional networks. However, these areas of significant difference were relatively sparse throughout the brain[5]. Meanwhile, longitudinal studies examining volume changes during adolescence in key subareas such as the hippocampus and amygdala have shown no difference between TD and ASD[6]. While there is ample evidence that differential neuroimaging features are present to differentiate ASD from TD, machine learning techniques have only achieved 80% ROC classification success from combined fMRI and structural data across the brain[7]. It has also been questioned if there are reliable sex differences in ASD or if observed sex-by-diagnosis interactions map to areas typically observed to show sex differences during development[8,9]. Studies on sex differences have suggested that ASD males and females may not exhibit sex-specific differences seen in typically developing individuals[10]; however, experimental parameters such as small sample sizes, lack of consistent experimental control factors, and a relative lack of female subjects have generally impacted many studies, making it difficult to gain insight on the neurobiological basis for ASD from an imaging perspective.

Connectomic Differences in ASD: Altered functional connectivity in the brain is a widely noted feature of ASD. However, functional connectivity alterations are not uniform across the brain and are associated with a brain-wide pattern of hypo- and hyperconnectivity depending on the active region being examined[11–14]. A mega-analysis of nearly 2000 individuals between 5-58 years old found that hypoconnectivity of the sensory

and attentional network and hyperconnectivity between cortical and subcortical systems were associated with clinically relevant autistic features such as social impairments, repetitive behavior, and sensory processing[11]. This pattern is potentially present in early childhood, as a recent study by Yoon et al. (2022) found lower network efficiencies and reduced longer-range anterior-posterior resting-state connectivity in 2-6 year-olds with ASD[13]. Results from functional connectivity studies led to the development of a cortical underconnectivity theory, which postulated that the observed differences resulted from a deficiency in the presence or function of longer-range distal connections and an overreliance on shorter-range or local connections[15–17]. While initially controversial[18], several studies have supplied a variety of functional evidence in agreement with this theory[12,19–22]. Structural data has also provided evidence supporting reduced long-distance connectivity, with the corpus callosum (key to long-distance inter-hemispheric connectivity), in autistic individuals having lower fiber counts and volumes than comparison TD participants[23]. While the functional evidence describes the consequences of altered brain connections, it is essential to develop microstructural evidence that may highlight neuronal processes that lead to altered function to evaluate the underconnectivity theory and provide insight into the neurobiological basis for ASD.

Neuronal Microstructure: If the underconnectivity theory of ASD is accurate, it is likely that observed functional connectivity changes have a basis in the cellular microstructure of the neurons. Diffusion models of cellular microstructure can provide detailed information on architectural changes in brain structure at the sub-voxel level and describe specific cellular milieu rather than gross anatomy. In this framework, lower directional diffusion, referred to as anisotropic, and higher adirectional diffusion, referred to as isotropic, may indicate deficits in axonal morphology that would cause reduced action potential speed or efficiency and drive reduced connectivity deficits. Depending on which axons and axonal areas are affected, this might impact particular systems or longer/shorter range connections, particularly since longer-range connections rely on larger and higher diameter axons to efficiently transmit information across the brain[24–26]. Previous diffusion microstructure experiments have demonstrated that ASD participants display different axonal anatomy compared to TD participants, such as structural differences in neuronal white matter (WM), with ASD being associated with lower fractional anisotropy (FA) and higher diffusivity[27]. Using NODDI, one study has found increased extracellular water and decreased neurite density in ASD throughout major tractography bundles in the brain[28,29]. Other work has applied constrained spherical deconvolution to examine differences in axonal volume between ASD and TD participants using fixel-based analysis. Here, a fixel refers to an individual fiber population within a voxel, derived from the WM-FODs calculated using constrained spherical deconvolution,

and allows for fiber-specific metric calculation relating to intra-axonal volume[30–33]. This analysis found that participants with ASD had significantly lower fiber density cross-section, a volume and fiber bundle diameter modified measure of intra-axonal volume, compared to TD participants across several major WM bundles of interest throughout the brain[27].

Neuroimaging-based Assessment of Neuronal Conduction Velocity: Beyond axonal fiber density, it is also possible to describe the relationship between axons and the myelin sheath surrounding them, providing the hallmark of the structural and diffusion microenvironment. The g-ratio is a quantitative proportion between axon diameter and myelin thickness first described by Rushton[34]. Increased myelin improves the resistivity of the axonal cellular membrane between the Nodes of Ranvier and provides for increased speed and energetic efficiency conducting action potentials[35,36]. Both axonal diameter and myelin thickness affect neuronal conduction velocity and spatial, energetic, and conductive properties within the human nervous system, leading to an optimal g-ratio of around 0.6-0.7[34,37,38]. The g-ratio thus describes a fundamental linkage between neurons' structure and function (via conduction velocity). Genetic[39,40], electrical[41–45], and functional[8,46–49] evidence suggests that neural activity is disrupted in ASD. Post-mortem histological studies also demonstrate that myelin and axons display abnormal morphology in ASD[50]. MRI-based measures of g-ratio, conduction velocity, and microstructural axonal properties are needed to establish *in vivo* measurements to give insights into the underpinnings of ASD.

Developing more sensitive models of microstructure and axonal properties may provide insight into structural and cellular processes in ASD. The g-ratio is an important measure of axonal integrity, and that accounts for axonal diameter and the diameter of the myelin sheath surrounding the axon[51,52]. Conduction velocity is an important metric that addresses the capacity of the axonal fiber to carry information, and this can be derived, in part, from the g-ratio[53]. The present study aims to establish novel means of calculating both these metrics, in aggregate form across all axonal fibers in a voxel, using a combination of diffusion and structural MRI and applying these metrics to an ASD cohort.

Methods:

Participants: Two-hundred seventy-three (mean age = 154.3 months ±35.21 S.D., 133 female [49%]) subjects from Wave 1 of an NIH-sponsored Autism Centers for Excellence Network were included in this study. The study cohort included 148 individuals diagnosed with ASD (mean age = 150.8 months ±34.31 S.D., 70 female [47%]) and 124 neurotypical participants (mean age = 154.3 months ±35.21 S.D., 62 female [50%]).

Image Acquisition: Diffusion, T1-weighted, and T2-weighted images were acquired from each subject. Diffusion images were acquired with an isotropic voxel size of 2x2x2mm, 64 non-colinear gradient directions at b=1000 s/mm2, and 1 b=0. T1-weighted MPRAGE images with a FOV of 176x256x256mm and an isotropic voxel size of 1x1x1mm, TE=3.3; T2-weighted images were acquired with a FOV of 128x128x34 with a voxel size of 1.5x1.5x4mm, TE=35.

Image Data Processing: A simple overview of the image processing pipeline, showing which imaging metrics contributed to calculation of other imaging metrics, is presented in Fig. 1. As described in Newman et al.[54], diffusion images were denoised[55], corrected for Gibbs ringing artifacts[56], and corrected for inhomogeneity fields using FSL's *topup* and *eddy* commands utilizing outlier detection and replacemnet[57–59], and the final preprocessed diffusion images were up-sampled to an isotropic voxel size of 1.3x1.3x1.3mm[60]. WM, GM, and CSF tissue response functions were generated using the *Dhollander* algorithm[61], and single-shell 3-tissue constrained spherical deconvolution was used to generate the WM fiber orientation distribution (FODs) and GM and CSF representations. 3-Tissue Constrained Spherical Deconvolution[62–65] was used to calculate the voxel-wise maps of the fraction of signal arising from each of 3 compartments: an intracellular anisotropic, intracellular isotropic, and extracellular isotropic freely diffusing water compartment by setting the sum of all FOD coefficients equal to unity. WM-FODs were then used to create a cohort-specific template with a subset of 40 individuals counterbalanced between sex and diagnosis[66]. All subject's WM-FODs were registered to this template using an affine non-linear transform warp, and then the template was registered to a b-value matched template in stereotaxic MNI space[67,68].

Estimating Axonal Fiber Diameter: A fixel-based morphometry (FBM)[30,31] approach was used to estimate the intra-axonal cross-sectional area within each voxel to be used as an apparent axonal volume fraction (AVF). FBM combines fiber density, computed from the integral of each WM-FOD spherical harmonic lobe, and cross-sectional area, computed using the Jacobian matrix determinant, which reflects the change in cross-sectional area when normalized to the template image. The cross-sectional change is used as a weight to the fiber density, and the two metrics are multiplied on a voxel-wise basis to obtain the fiber density cross-section related to the total intra-axonal volume (AVF)[30,33]. Each subject's AVF maps were then registered to MNI space using the ANTs SyN nonlinear registration technique by aligning each to the 11-year-old adolescent template developed by Richards et al. Note a template approximately 1 standard deviation below the mean age of this study was used to better register the comparatively much smaller younger subjects[69,70].

Myelination Density: T1w and T2w images were processed as described in the MICA-MNI pipeline[71]; this involved performing N4 bias correction from ANTs[72,73] on both T1w and T2w images, rescaling both images from 0-100 based on their maximum values, co-registering the T2w to the T1w image using ANTs[73] rigid registration and then calculating the T1/T2 ratio on a voxel-wise basis[74]. T1/T2 ratio images were then registered to MNI space using the ANTs SyN nonlinear registration technique by aligning each to the same Richards et al. templates used to register the AVF maps.

Conduction Velocity Determination: The aggregate g-ratio was calculated on a voxel-wise basis according to Stikov et al. and was used according to Mohammadi & Callaghan as displayed in Equation 1[51,52,75,76]. As a measure of intra-axonal volume, the fiber density cross section was used as the AVF[31], and as a metric of myelin density, the T1/T2 ratio was used as the myelin volume fraction (MVF). Both of these metrics represent the total sums of each respective compartment across the volume of the voxel and are a volume-based equivalent to the original formulation of g as the ratio of axon diameter (d) to fiber diameter (D).

$$g = \frac{d}{D} = \sqrt{1 - \frac{MVF}{MVF+AVF}} \tag{1}$$

Aggregate conduction velocity was calculated based on the calculations of Rushton[34] and Berman et al.[53]; reiterating Rushton's calculation that conduction velocity (θ) is proportional to the length of each fiber segment (l), and that this is roughly proportional to *D,* which in turn can be defined as the ratio between *d* and the g-ratio (g). Furthering the considerations of Rushton, Berman et al. show that a value proportional to conduction velocity can be calculated using axon diameter and the g-ratio as in equation 2[53]:

$$\theta \propto l \propto Dg\sqrt{-\ln(g)} \propto d\sqrt{-\ln(g)} \tag{2}$$

Herein, aggregate conduction velocity is calculated at the whole-voxel level, similar to Stikov et al.'s original conceptualization of an aggregate g-ratio, with each voxel representing an ensemble of g-ratios within each individual axonal segment with arbitrary orientation. Thus, instead of axonal diameter, this study utilized a function of the arbitrarily oriented ensemble of intra-axonal volumes, returning to the AVF. It follows that increased or decreased diameter *in aggregate throughout a voxel* is proportional to intra-axonal volume.

All imaging metrics, 3T-CSD signal fraction compartments, T1/T2 ratio, aggregate g-ratio, and aggregate conduction velocity (Fig. 2) were averaged across each of 214 ROIs taken from the JHU-ICBM WM atlas (48 ROIs)[77] and the Destrieux Cortical Atlas (164 ROIs)[78]. Additionally, two composite ROIs were included, one of all 48 JHU ROIs and one of 150 neocortical regions from the Destrieux Atlas.

Statistical Approach: General linear models were used to test the relationship between each microstructural metric (intracellular anisotropic, intracellular isotropic, extracellular free water, T1/T2 ratio, aggregate g-ratio, and aggregate conduction velocity) on diagnosis and sex differences. All models featured subject age, IQ, scanner/site, and intracranial volume as control terms. All sets of microstructural results were corrected for multiple comparisons using the Benjamini & Hochberg (1995)[79] method across all 214 ROIs.

Results:

Given how the aggregate g-ratio and aggregate conduction velocity metrics were derived from diffusion and T1/T2 ratio information, these metrics were first compared using linear models across all 214 ROIs with subsequent Benjamini and Hochberg correction for multiple comparisons. These results can be viewed in Fig. 3, and as expected, the methods derived from T1/T2 ratio tended to be largely in agreement in both axonal ROIs from the JHU-ICBM atlas and in cortical ROIs from the Destrieux atlas. There were also many ROIs in the axonal areas where the ICA signal fraction was significantly associated with T1/T2 ratio. This is especially notable as the WM-FODs that contribute to the ICA signal fraction are used to derive the fixel-based estimate of AVF. However, far less significant associations existed between ICA and either aggregate g-ratio or aggregate conduction velocity. In the cortex, there was a widespread negative association between ECI (extracellular water) signal fraction and aggregate g-ratio and aggregate conduction velocity, suggesting that in this adolescent cohort, the intra-axonal volume mediates the volume of extracellular space in the cortex.

These metrics were then assessed using the full model for relationships to variables of interest. For full summarized results of all adjusted p-values, see Table 1, for raw means from each metric in every ROI, see Supplementary Table 1. Following multiple comparison corrections, 93 ROIs were found to have significantly greater extracellular water signal fraction in individuals with ASD compared to TD participants (Fig. 4), including in both composite ROIs covering the WM and neocortex. The significant ROIs were almost entirely located in the cortex, and no individual JHU-ICBM WM atlas ROIs, other than the entire composite ROI, survived multiple comparison corrections (Fig. 5). 7 ROIs located in the subcortical gray matter also displayed significantly greater extracellular water signal in ASD compared to participants. These included the Nucleus Accumbens, Hippocampus, and Thalamus on the left exclusively, and bilateral caudate and putamen. Areas

with the strongest relationship between extracellular water signal and ASD were the bilateral caudate nuclei and a bilateral series of pre- and post-central gyri in the parietal, superior temporal, and superior frontal lobes (Fig. 4).

Sixty-one ROIs were found to have significantly reduced aggregate g-ratio in ASD compared to TD participants (Fig. 4), including the composite WM ROI but not the composite cortical ROI (Fig. 5). Significant ROIs were located throughout the neocortex and axonal areas but were especially prominent in the superior parietal lobe. Only three subcortical areas showed significant differences, the right and left thalamus and the right nucleus accumbens.

One-hundred and fifty-five ROIs were found to have significantly reduced aggregate conduction velocity in ASD compared to TD participants (Fig. 4), including both composite ROIs in the neocortex and WM (Fig. 5). Significant ROIs included the majority of both atlases, with widespread associations between diagnosis and aggregate conduction velocity. Subcortically, there were significant associations with the bilateral amygdala, caudate, putamen, thalamus, and the right hippocampus. There was also a strong positive association between aggregate conduction velocity and IQ, with 206 ROIs surviving multiple comparison corrections, including every WM ROI from the ICBM-JHU-WM atlas. Four of the non-significant ROIs were the bilateral temporal and occipital poles, and the remaining three were the left inferior occipital gyrus and sulcus, the right lunate sulcus, and the right lateral orbital sulcus. Receiver operator characteristic (ROC) analysis was performed using the 'pROC' package in RStudio on the linear model for each composite ROI to determine which microstructural metric with significant ROIs was most sensitive and specific in regards to subject diagnosis (Fig. 6)[80]. The ECI signal fraction within the composite WM ROI had the highest area under the ROC curve (AUC), indicating the best sensitivity and specificity to diagnosis.

In regard to diagnosis, no other microstructure metric survived multiple comparison corrections in any ROI, including T1/T2 ratio. There was no significant effect of sex or of sex-by-diagnosis interaction in any ROI after multiple comparison corrections (Fig. 7). Though there were no significant associations with sex in any microstructural metric in any ROI, diagnosis groups show varying relationships with age that are not consistent across sexes, with far higher T1/T2 ratio values in TD males compared TD females, while in ASD, females tend to have higher T1/T2 ratio, and ECI signal fraction values compared to males. ASD males, meanwhile, tend to have higher ICI (GM-like) signal fraction values, while in TD participants, age-associated ROIs tend to have higher ICI (GM-like) values in females. Aggregate conduction velocity and aggregate g-ratio do not seem to

differ between ASD and TD in their age-by-sex interaction, despite having many significantly different ROIs between ASD and TD participants.

Discussion:

This study's results support the underconnectivity theory in ASD by describing for the first time subcellular findings that could be the neurobiological basis for reduced long-range connectivity[15–17]. This study reveals widespread significant mean differences between ASD and TD participants while also highlighting significant sex-dependent differences in brain structure compared to same-sex participants. These findings were primarily located in the neocortex in the ECI signal fraction, in the axonal WM areas for aggregate g-ratio, and in both neocortex and axonal WM areas for aggregate conduction velocity.

Multiple studies have previously described consistent increases in cortical thickness[2,4,81] and mean diffusivity with corresponding decreases in FA[82–84] in ASD compared to TD participants. Against this background, the widespread increases of extracellular water in cortical ROIs and decreased aggregate conduction velocity and aggregate g-ratio observed in this study can potentially be interpreted as widespread problems with myelination or as the microstructural result of increased cortical thickness. However, there was no significant difference in T1/T2 ratio (used as the MVF in this study) between ASD and TD, implying that there is a more complex relationship between myelination and ASD than simply a deficit compared to TD. By weighting intra-axonal volume (measured via the total sum of FDC) into both aggregate g-ratio and aggregate conduction velocity, it is possible that differences are driven by changes to axonal morphology at the sub-cellular level. This may be an architectural difference in cellular microstructure (i.e., axons themselves may be thinner or more dispersed in ASD), or, combined with the increased extracellular water exclusively in the cortex, there is increased active or previous neuroinflammation that stunted axonal and myelin development, leaving a sparser and higher volume cortex with a large portion of that increase simply being extracellular space. This finding is supported by the finding of increased extracellular water and decreased neuronal dispersion by other diffusion models such as NODDI[29].

Histological work performed on a small sample of WM from both TD and ASD adults found that superficial and deep WM had significantly more small axonal fibers and significantly more branching axonal fibers in ASD compared to TD participants[50]. Individuals with ASD also had significantly thinner myelin sheaths in all sizes of axon[50]. Though this histological experiment was performed in adults instead of the adolescents in this study, given these two factors, a bias toward smaller diameter axons and thinner myelin, it is likely that the results reported here confirm this prior finding, as the aggregate g-ratio in this adolescent cohort is overall

lower than expected in adults due to insufficiently developed myelin, and thus the TD group can be interpreted as nearer to developed myelin and thus higher g-ratio closer to optimum values[52,76,85,86]. It has also been reported that children with ASD have lower conduction velocity using magnetoencephalography[87,88] and in peripheral neurons[89], potentially due to reduced axonal diameter and the prevalence of small fibers. This study reinforces this finding by showing widespread reduced aggregate conduction velocity in ASD throughout the brain. The observed reductions in aggregate conduction velocity, in particular, may indicate deficits, particularly in longer-range axonal connections dependent on higher-diameter fibers and myelination. This effect was observed in both aggregate g-ratio and aggregate conduction velocity throughout a wide range of the axonal skeleton, indicating that these functional deficits are systemic.

It should also be noted that extensive work has shown that extracellular water increases in the axonal WM skeleton with age and cerebrovascular injury[64,90–92], but that none of the axonal ROIs tested was significant for ECI signal fraction differences, suggesting that there is no active degeneration of brain cells or microstructure. The findings of extracellular water differences exclusively in cortex pairs with the lack of findings in the axonal signal compartment and in the T1/T2 ratio measurement of myelin in any ROIs examined. This is also an important reminder that T2-weighted signal and extracellular water are not interchangeable, especially in development. The water in the extracellular space is still close to the bound volume fraction pool water, and the T2-weighted signal was increased enough compared to the T1-weighted signal to serve as a marker of ASD in the T1/T2 ratio metric. Note, however, that the ECI signal fraction had the highest number of negative correlations with g-ratio and conduction velocity, but, as expected, those metrics were closely related to T1/T2 ratio in nearly every ROI, despite T1/T2 ratio subsequently having no ROIs that were different between ASD and TD participants. An additional possibility is that changes in synaptic formation as suggested by several genetic associations between ASD and growth-cone-related genes such as CRMP1 and CRMP2[93]. Recent work using FDC in other model systems, such as the optic nerve, has suggested that fiber cross-section may be a key component of information transfer and downstream neuronal development[94]. Validation studies in animal models or via further histopathological study are required to further investigate the cellular basis of these observed effects.

Conclusion:

Advanced diffusion and structural microstructure models can characterize a combination of increased extracellular water and decreased aggregate g-ratio and aggregate conduction velocity between ASD and TD

participants. This study introduces a novel means to calculate aggregate g-ratio using diffusion MRI techniques and a novel calculation of aggregate conduction velocity as well as applying both to the study of ASD for the first time. These findings suggest that differences in axon morphology are widespread throughout the brain which may underlie ASD, generally, beget altered signal transduction along affected fiber pathways, thus providing an explanation for recent observations of local versus distal connection dependencies more specifically in those diagnosed with ASD.

Acknowledgements:

This work was performed on behalf of the GENDAAR Consortium (NIH R01 MH100028), and we thank all of our collaborating colleagues, the study participants, and their family members. We would like to specifically acknowledge the contributions of Anna Kresse, MPH; Megha Santhosh, MHA; Désirée Lussier-Lévesque, PhD; Emily Neuhaus, PhD; Katy Ankenman, MSW; Jessica Benton, MA; and Rachel Fung, BS.

Conflicts of Interest:

James C. McPartland consults with Customer Value Partners, Bridgebio, Determined Health, and BlackThorn Therapeutics, has received research funding from Janssen Research and Development, serves on the Scientific Advisory Boards of Pastorus and Modern Clinics, and receives royalties from Guilford Press, Lambert, Oxford, and Springer. Other authors declare no conflicts of interest.

Authorship Contributions:

BTN conducted the analyses and wrote the manuscript; ZJ curated the data sets used in the analyses; SV contributed to the theoretical concepts; JDVH conceived of the study, contributed to the theoretical considerations, and helped to write the manuscript; KAP provided leadership; SJW, NAK, KAP, and JCM provided expertise in ASD clinical assessment and neurophysiological research.

References:

1. Werling DM, Geschwind DH. Sex differences in autism spectrum disorders. *Current opinion in neurology*. 2013;26(2):146.

2. Brambilla P, Hardan A, Di Nemi SU, Perez J, Soares JC, Barale F. Brain anatomy and development in autism: review of structural MRI studies. *Brain research bulletin*. 2003;61(6):557-569.

3. Chen R, Jiao Y, Herskovits EH. Structural MRI in autism spectrum disorder. *Pediatric research*. 2011;69(8):63-68.

4. Khundrakpam BS, Lewis JD, Kostopoulos P, Carbonell F, Evans AC. Cortical thickness abnormalities in autism spectrum disorders through late childhood, adolescence, and adulthood: a large-scale MRI study. *Cerebral Cortex*. 2017;27(3):1721-1731.

5. Pua EPK, Ball G, Adamson C, Bowden S, Seal ML. Quantifying individual differences in brain morphometry underlying symptom severity in Autism Spectrum Disorders. *Scientific Reports*. 2019;9(1):1-10.

6. Barnea-Goraly N, Frazier TW, Piacenza L, et al. A preliminary longitudinal volumetric MRI study of amygdala and hippocampal volumes in autism. *Progress in Neuro-Psychopharmacology and Biological Psychiatry*. 2014;48:124-128.

7. Mellema CJ, Nguyen KP, Treacher A, Montillo A. Reproducible neuroimaging features for diagnosis of autism spectrum disorder with machine learning. *Scientific reports*. 2022;12(1):3057.

8. Walsh MJ, Wallace GL, Gallegos SM, Braden BB. Brain-based sex differences in autism spectrum disorder across the lifespan: A systematic review of structural MRI, fMRI, and DTI findings. *NeuroImage: Clinical*. 2021;31:102719.

9. Ritchie SJ, Cox SR, Shen X, et al. Sex differences in the adult human brain: evidence from 5216 UK biobank participants. *Cerebral cortex*. 2018;28(8):2959-2975.

10. Peterson BS, Liu J, Dantec L, et al. Using tissue microstructure and multimodal MRI to parse the phenotypic heterogeneity and cellular basis of autism spectrum disorder. *Journal of Child Psychology and Psychiatry*. 2022;63(8):855-870.

11. Ilioska I, Oldehinkel M, Llera A, et al. Connectome-wide mega-analysis reveals robust patterns of atypical functional connectivity in autism. *Biological Psychiatry*. Published online 2022.

12. Jao Keehn RJ, Nair S, Pueschel EB, Linke AC, Fishman I, Müller RA. Atypical local and distal patterns of occipito-frontal functional connectivity are related to symptom severity in autism. *Cerebral Cortex*. 2019;29(8):3319-3330.

13. Yoon N, Huh Y, Lee H, et al. Alterations in Social Brain Network Topology at Rest in Children With Autism Spectrum Disorder. *Psychiatry Investigation*. 2022;19(12):1055-1068.

14. Hull JV, Dokovna LB, Jacokes ZJ, Torgerson CM, Irimia A, Van Horn JD. Resting-state functional connectivity in autism spectrum disorders: a review. *Frontiers in psychiatry*. 2017;7:205.

15. Just MA, Keller TA, Malave VL, Kana RK, Varma S. Autism as a neural systems disorder: a theory of frontal-posterior underconnectivity. *Neuroscience & Biobehavioral Reviews*. 2012;36(4):1292-1313.

16. Just MA, Cherkassky VL, Keller TA, Minshew NJ. Cortical activation and synchronization during sentence comprehension in high-functioning autism: evidence of underconnectivity. *Brain*. 2004;127(8):1811-1821.

17. Just MA, Cherkassky VL, Keller TA, Kana RK, Minshew NJ. Functional and anatomical cortical underconnectivity in autism: evidence from an FMRI study of an executive function task and corpus callosum morphometry. *Cerebral cortex*. 2007;17(4):951-961.

18. Picci G, Gotts SJ, Scherf KS. A theoretical rut: revisiting and critically evaluating the generalized under/over-connectivity hypothesis of autism. *Developmental science*. 2016;19(4):524-549.

19. Curl A, Coderre EL. The time-locked neurodynamics of semantic processing in autism spectrum disorder: an EEG study. *Cognitive Neurodynamics*. Published online 2022:1-30.

20. Trapani JA, Bednarz HM, Kana RK. Brain function and brain connectivity in autism. In: *The Neuroscience of Autism*. Elsevier; 2022:107-126.

21. Carroll L, Braeutigam S, Dawes JM, et al. Autism spectrum disorders: multiple routes to, and multiple consequences of, abnormal synaptic function and connectivity. *The Neuroscientist*. 2021;27(1):10-29.

22. Keehn RJJ, Pueschel EB, Gao Y, et al. Underconnectivity between visual and salience networks and links with sensory abnormalities in autism spectrum disorders. *Journal of the American Academy of Child & Adolescent Psychiatry*. 2021;60(2):274-285.

23. Nickel K, Perlov E, Reisert M, et al. Altered transcallosal fiber count and volume in high-functioning adults with autism spectrum disorder. *Psychiatry Research: Neuroimaging*. 2022;322:111464.

24. Liewald D, Miller R, Logothetis N, Wagner HJ, Schüz A. Distribution of axon diameters in cortical white matter: an electron-microscopic study on three human brains and a macaque. *Biological cybernetics*. 2014;108:541-557.

25. Stepanyants A, Martinez LM, Ferecskó AS, Kisvárday ZF. The fractions of short-and long-range connections in the visual cortex. *Proceedings of the National Academy of Sciences*. 2009;106(9):3555-3560.

26. Das A, Gilbert CD. Long-range horizontal connections and their role in cortical reorganization revealed by optical recording of cat primary visual cortex. *Nature*. 1995;375(6534):780-784.

27. Dimond D, Schuetze M, Smith RE, et al. Reduced white matter fiber density in autism spectrum disorder. *Cerebral Cortex*. 2019;29(4):1778-1788.

28. Zhang H, Schneider T, Wheeler-Kingshott CA, Alexander DC. NODDI: practical in vivo neurite orientation dispersion and density imaging of the human brain. *Neuroimage*. 2012;61(4):1000-1016.

29. Andica C, Kamagata K, Kirino E, et al. Neurite orientation dispersion and density imaging reveals white matter microstructural alterations in adults with autism. *Molecular Autism*. 2021;12(1):1-14.

30. Raffelt DA, Tournier JD, Smith RE, et al. Investigating white matter fibre density and morphology using fixel-based analysis. *Neuroimage*. 2017;144:58-73.

31. Raffelt D, Tournier JD, Rose S, et al. Apparent fibre density: a novel measure for the analysis of diffusion-weighted magnetic resonance images. *Neuroimage*. 2012;59(4):3976-3994.

32. Raffelt DA, Smith RE, Ridgway GR, et al. Connectivity-based fixel enhancement: Whole-brain statistical analysis of diffusion MRI measures in the presence of crossing fibres. *Neuroimage*. 2015;117:40-55.

33. Dhollander T, Clemente A, Singh M, et al. Fixel-based analysis of diffusion MRI: methods, applications, challenges and opportunities. *Neuroimage*. 2021;241:118417.

34. Rushton WAH. A theory of the effects of fibre size in medullated nerve. *The Journal of physiology*. 1951;115(1):101.

35. Hodgkin AL, Huxley AF. A quantitative description of membrane current and its application to conduction and excitation in nerve. *The Journal of physiology*. 1952;117(4):500.

36. Häusser M. The Hodgkin-Huxley theory of the action potential. *Nature neuroscience*. 2000;3(11):1165-1165.

37. Gillespie MJ, Stein RB. The relationship between axon diameter, myelin thickness and conduction velocity during atrophy of mammalian peripheral nerves. *Brain research*. 1983;259(1):41-56.

38. Gasser HS, Grundfest H. Axon diameters in relation to the spike dimensions and the conduction velocity in mammalian A fibers. *American Journal of Physiology-Legacy Content*. 1939;127(2):393-414.

39. Walsh CA, Morrow EM, Rubenstein JL. Autism and brain development. *Cell*. 2008;135(3):396-400.

40. Willsey HR, Willsey AJ, Wang B, State MW. Genomics, convergent neuroscience and progress in understanding autism spectrum disorder. *Nature Reviews Neuroscience*. 2022;23(6):323-341.

41. Gabard-Durnam LJ, Wilkinson C, Kapur K, Tager-Flusberg H, Levin AR, Nelson CA. Longitudinal EEG power in the first postnatal year differentiates autism outcomes. *Nature communications*. 2019;10(1):4188.

42. Pham TH, Vicnesh J, Wei JKE, et al. Autism spectrum disorder diagnostic system using HOS bispectrum with EEG signals. *International journal of environmental research and public health*. 2020;17(3):971.

43. Tawhid MNA, Siuly S, Wang H, Whittaker F, Wang K, Zhang Y. A spectrogram image based intelligent technique for automatic detection of autism spectrum disorder from EEG. *Plos one*. 2021;16(6):e0253094.

44. Levisohn PM. The autism-epilepsy connection. *Epilepsia*. 2007;48:33-35.

45. Oberman LM, Hubbard EM, McCleery JP, Altschuler EL, Ramachandran VS, Pineda JA. EEG evidence for mirror neuron dysfunction in autism spectrum disorders. *Cognitive brain research*. 2005;24(2):190-198.

46. Philip RC, Dauvermann MR, Whalley HC, Baynham K, Lawrie SM, Stanfield AC. A systematic review and meta-analysis of the fMRI investigation of autism spectrum disorders. *Neuroscience & Biobehavioral Reviews*. 2012;36(2):901-942.

47. Koshino H, Carpenter PA, Minshew NJ, Cherkassky VL, Keller TA, Just MA. Functional connectivity in an fMRI working memory task in high-functioning autism. *Neuroimage*. 2005;24(3):810-821.

48. Karunakaran P, Hamdan YB. Early prediction of autism spectrum disorder by computational approaches to fMRI analysis with early learning technique. *Journal of Artificial Intelligence*. 2020;2(04):207-216.

49. Dekhil O, Ali M, Haweel R, et al. A comprehensive framework for differentiating autism spectrum disorder from neurotypicals by fusing structural MRI and resting state functional MRI. In: *Seminars in Pediatric Neurology*. Vol 34. Elsevier; 2020:100805.

50. Zikopoulos B, Barbas H. Changes in Prefrontal Axons May Disrupt the Network in Autism. *J Neurosci*. 2010;30(44):14595-14609. doi:10.1523/JNEUROSCI.2257-10.2010

51. Campbell JS, Leppert IR, Narayanan S, et al. Promise and pitfalls of g-ratio estimation with MRI. *Neuroimage*. 2018;182:80-96.

52. Mohammadi S, Callaghan MF. Towards in vivo g-ratio mapping using MRI: Unifying myelin and diffusion imaging. *Journal of neuroscience methods*. 2021;348:108990.

53. Berman S, Filo S, Mezer AA. Modeling conduction delays in the corpus callosum using MRI-measured g-ratio. *Neuroimage*. 2019;195:128-139.

54. Newman BT, Dhollander T, Reynier KA, Panzer MB, Druzgal TJ. Test–retest reliability and long-term stability of three-tissue constrained spherical deconvolution methods for analyzing diffusion MRI data. *Magn Reson Med*. 2020;84(4):2161-2173. doi:10.1002/mrm.28242

55. Veraart J, Novikov DS, Christiaens D, Ades-Aron B, Sijbers J, Fieremans E. Denoising of diffusion MRI using random matrix theory. *Neuroimage*. 2016;142:394-406.

56. Kellner E, Dhital B, Kiselev VG, Reisert M. Gibbs-ringing artifact removal based on local subvoxel-shifts. *Magnetic resonance in medicine*. 2016;76(5):1574-1581.

57. Andersson JL, Sotiropoulos SN. An integrated approach to correction for off-resonance effects and subject movement in diffusion MR imaging. *Neuroimage*. 2016;125:1063-1078.

58. Andersson JL, Graham MS, Zsoldos E, Sotiropoulos SN. Incorporating outlier detection and replacement into a non-parametric framework for movement and distortion correction of diffusion MR images. *Neuroimage*. 2016;141:556-572.

59. Andersson JL, Skare S, Ashburner J. How to correct susceptibility distortions in spin-echo echo-planar images: application to diffusion tensor imaging. *Neuroimage*. 2003;20(2):870-888.

60. Greenspan H. Super-resolution in medical imaging. *The computer journal*. 2009;52(1):43-63.

61. Dhollander T, Raffelt D, Connelly A. Unsupervised 3-tissue response function estimation from single-shell or multi-shell diffusion MR data without a co-registered T1 image. In: *ISMRM Workshop on Breaking the Barriers of Diffusion MRI*. Vol 5. ISMRM; 2016.

62. Dhollander T, Raffelt D, Connelly A. Towards interpretation of 3-tissue constrained spherical deconvolution results in pathology. In: *Proc. Intl. Soc. Mag. Reson. Med*. Vol 25. ; 2017:1815.

63. Mito R, Dhollander T, Xia Y, et al. In vivo microstructural heterogeneity of white matter lesions in healthy elderly and Alzheimer's disease participants using tissue compositional analysis of diffusion MRI data. *NeuroImage: Clinical*. 2020;28:102479.

64. Mito R, Dhollander T, Raffelt D, et al. Investigating microstructural heterogeneity of white matter hyperintensities in Alzheimer's disease using single-shell 3-tissue constrained spherical deconvolution. In: *Proc. Intl. Soc. Mag. Reson. Med*. ; 2018:135.

65. Kelly C, Dhollander T, Harding IH, et al. Brain tissue microstructural and free-water composition 13 years after very preterm birth. *Neuroimage*. 2022;254:119168.

66. Raffelt D, Tournier JD, Crozier S, Connelly A, Salvado O. Reorientation of fiber orientation distributions using apodized point spread functions. *Magnetic resonance in medicine*. 2012;67(3):844-855.

67. Hsu YC, Lo YC, Chen YJ, Wedeen VJ, Isaac Tseng WY. NTU-DSI-122: A diffusion spectrum imaging template with high anatomical matching to the ICBM-152 space. *Human brain mapping*. 2015;36(9):3528-3541.

68. Newman BT, Untaroiu A, Druzgal TJ. A novel diffusion registration method with the NTU-DSI-122 template to transform free water signal fraction maps to stereotaxic space. 2020;Proceedings of the ISMRM 28th General Meeting.

69. Richards JE, Xie W. Brains for all the ages: structural neurodevelopment in infants and children from a life-span perspective. *Advances in child development and behavior*. 2015;48:1-52.

70. Richards JE, Sanchez C, Phillips-Meek M, Xie W. A database of age-appropriate average MRI templates. *Neuroimage*. 2016;124:1254-1259.

71. Cruces RR, Royer J, Herholz P, et al. Micapipe: A pipeline for multimodal neuroimaging and connectome analysis. *NeuroImage*. 2022;263:119612.

72. Avants BB, Tustison N, Song G. Advanced normalization tools (ANTS). *Insight j*. 2009;2(365):1-35.

73. Avants BB, Tustison NJ, Stauffer M, Song G, Wu B, Gee JC. The Insight ToolKit image registration framework. *Front Neuroinform*. 2014;8. doi:10.3389/fninf.2014.00044

74. Glasser MF, Van Essen DC. Mapping human cortical areas in vivo based on myelin content as revealed by T1-and T2-weighted MRI. *Journal of neuroscience*. 2011;31(32):11597-11616.

75. Stikov N, Perry LM, Mezer A, et al. Bound pool fractions complement diffusion measures to describe white matter micro and macrostructure. *Neuroimage*. 2011;54(2):1112-1121.

76. Stikov N, Campbell JS, Stroh T, et al. In vivo histology of the myelin g-ratio with magnetic resonance imaging. *Neuroimage*. 2015;118:397-405.

77. Mori S, Wakana S, Van Zijl PC, Nagae-Poetscher LM. *MRI Atlas of Human White Matter*. Elsevier; 2005.

78. Destrieux C, Fischl B, Dale A, Halgren E. Automatic parcellation of human cortical gyri and sulci using standard anatomical nomenclature. *Neuroimage*. 2010;53(1):1-15.

79. Benjamini Y, Hochberg Y. Controlling the false discovery rate: a practical and powerful approach to multiple testing. *Journal of the Royal statistical society: series B (Methodological)*. 1995;57(1):289-300.

80. Robin X, Turck N, Hainard A, et al. pROC: an open-source package for R and S+ to analyze and compare ROC curves. *BMC bioinformatics*. 2011;12(1):1-8.

81. Yang DYJ, Beam D, Pelphrey KA, Abdullahi S, Jou RJ. Cortical morphological markers in children with autism: a structural magnetic resonance imaging study of thickness, area, volume, and gyrification. *Molecular autism*. 2016;7(1):1-14.

82. Zhao Y, Yang L, Gong G, Cao Q, Liu J. Identify aberrant white matter microstructure in ASD, ADHD and other neurodevelopmental disorders: A meta-analysis of diffusion tensor imaging studies. *Progress in Neuro-Psychopharmacology and Biological Psychiatry*. 2022;113:110477.

83. Schadler A. *Detection of Tract-Specific White Matter Compromise in Adolescents with Autism Spectrum Disorders Using an Automated Tractography Pipeline*. PhD Thesis. San Diego State University; 2021.

84. Valenti M, Pino MC, Mazza M, Panzarino G, Di Paolantonio C, Verrotti A. Abnormal structural and functional connectivity of the corpus callosum in autism spectrum disorders: A review. *Review Journal of Autism and Developmental Disorders*. 2020;7:46-62.

85. Paus T. Growth of white matter in the adolescent brain: myelin or axon? *Brain and cognition*. 2010;72(1):26-35.

86. Genc S, Raven EP, Drakesmith M, Blakemore SJ, Jones DK. Novel insights into axon diameter and myelin content in late childhood and adolescence. *Cerebral Cortex*. Published online January 4, 2023:bhac515. doi:10.1093/cercor/bhac515

87. Roberts TPL, Bloy L, Ku M, et al. A Multimodal Study of the Contributions of Conduction Velocity to the Auditory Evoked Neuromagnetic Response: Anomalies in Autism Spectrum Disorder. *Autism Research*. 2020;13(10):1730-1745. doi:10.1002/aur.2369

88. Berman JI, Edgar JC, Blaskey L, et al. Multimodal Diffusion-MRI and MEG Assessment of Auditory and Language System Development in Autism Spectrum Disorder. *Front Neuroanat*. 2016;10. doi:10.3389/fnana.2016.00030

89. Chien YL, Chao CC, Wu SW, et al. Small fiber pathology in autism and clinical implications. *Neurology*. 2020;95(19):e2697-e2706. doi:10.1212/WNL.0000000000010932

90. Newman BT, Danoff JS, Lynch ME, et al. Epigenetic age acceleration predicts subject-specific white matter degeneration in the human brain. *bioRxiv*. Published online 2022:2022.11. 14.516491.

91. Blair J C, Newman BT, Druzgal TJ. Evaluating Lifespan Tissue Structure: Comparing CSD Signal Fraction and VBM Grey Matter Density. *Proceedings of the ISMRM 27th General Meeting*. Published online 2019.

92. Khan W, Khlif MS, Mito R, Dhollander T, Brodtmann A. Investigating the microstructural properties of normal-appearing white matter (NAWM) preceding conversion to white matter hyperintensities (WMHs) in stroke survivors. *NeuroImage*. 2021;232:117839.

93. Ramirez-Celis A, Becker M, Nuño M, Schauer J, Aghaeepour N, Van de Water J. Risk assessment analysis for maternal autoantibody-related autism (MAR-ASD): a subtype of autism. *Molecular psychiatry*. 2021;26(5):1551-1560.

94. Taskin HO, Qiao Y, Sydnor VJ, et al. Retinal ganglion cell endowment is correlated with optic tract fiber cross section, not density. *NeuroImage*. 2022;260:119495. doi:10.1016/j.neuroimage.2022.119495

Figures:

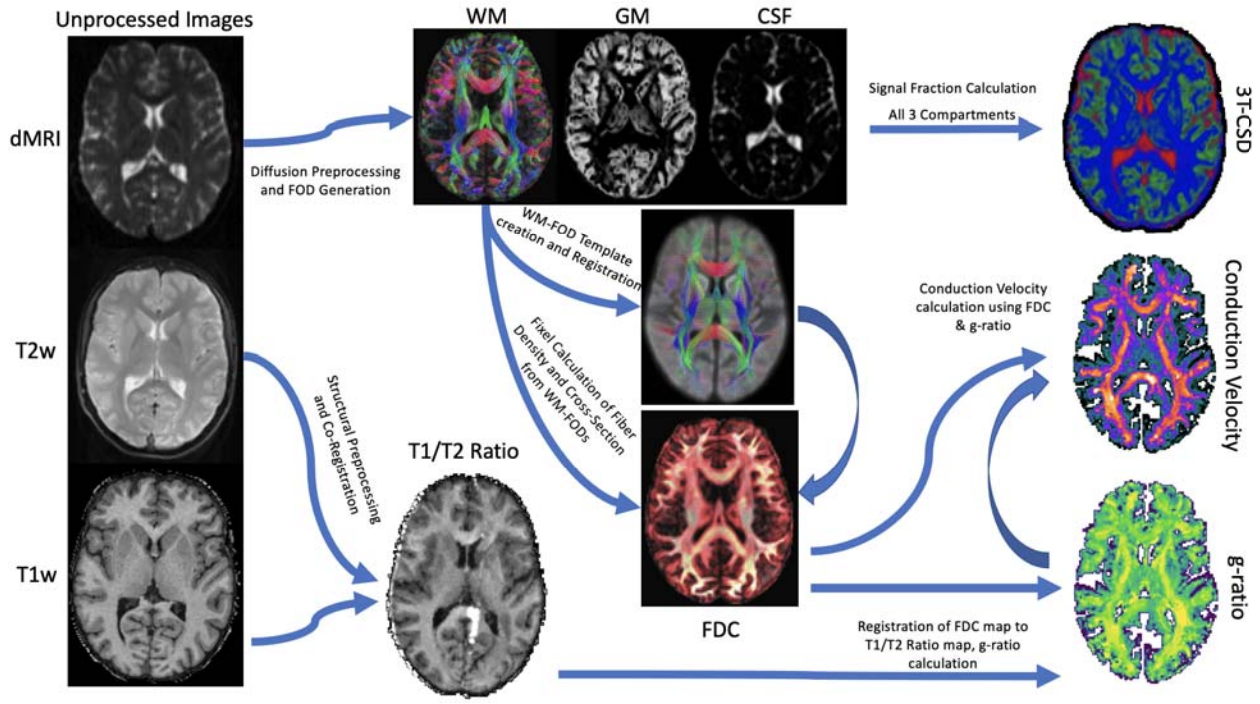

Figure 1: Simple flow diagram displaying which imaging metrics contributed to which output metrics. Fiber density cross-section (FDC) was derived from WM-FODs as part of a fixel analysis pipeline, then summed voxel-wise as an intra-axonal volume fraction (AVF) estimate while T1/T2 ratio was used as a myelin volume fraction (MVF) for the calculation of g-ratio and conduction velocity. It should also be noted that 3T-CSD metrics were separately registered to the MNI space atlases via a different procedure than the metrics derived from T1/T2 ratio.

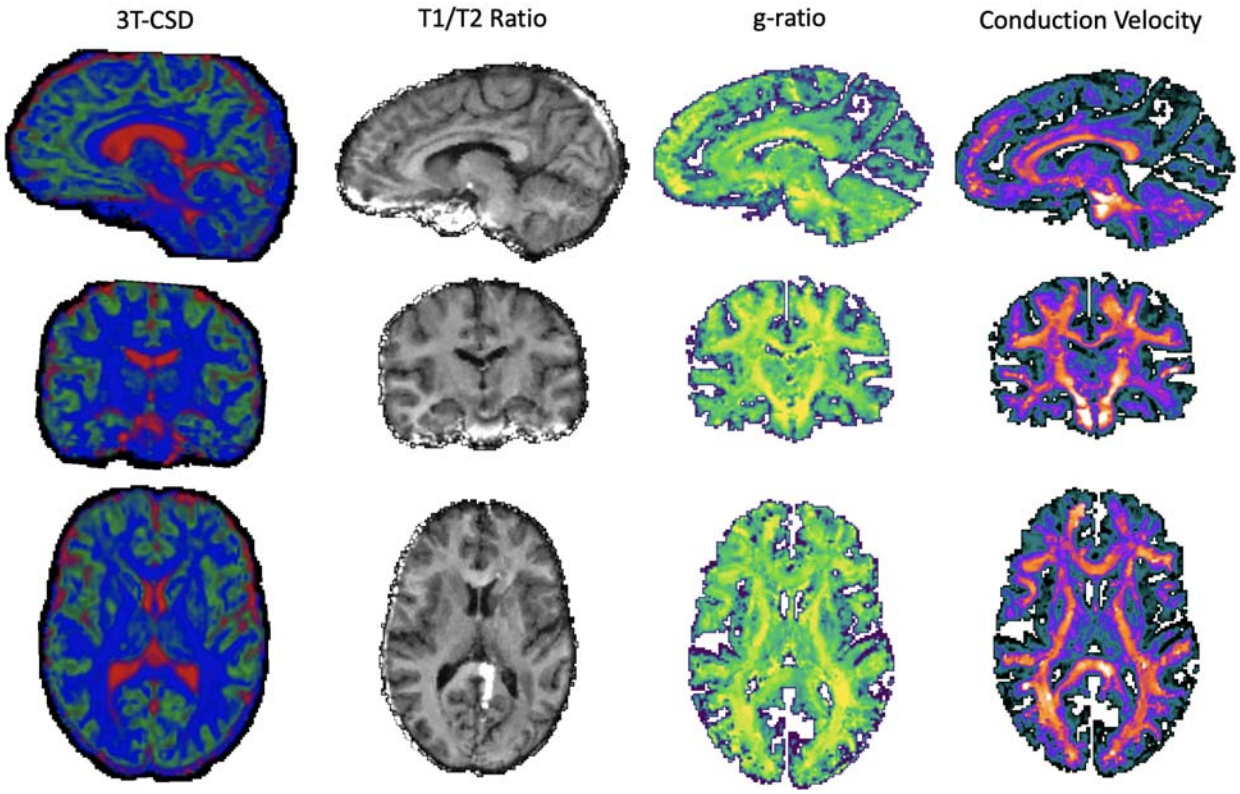

Figure 2: Illustration of each brain cellular microstructure metric from a single individual in this study. 3T-CSD is displayed as a composite of each of the 3 constituent tissue compartments having a value for each voxel, with blue voxels representing majority ICA (WM-like) signal, green voxels representing majority ICI (GM-like) signal, and red representing majority ECI (extracellular free water) signal. T1/T2 ratio, aggregate g-ratio, and aggregate conduction velocity are colored with arbitrary scales to emphasize differences between brain areas.

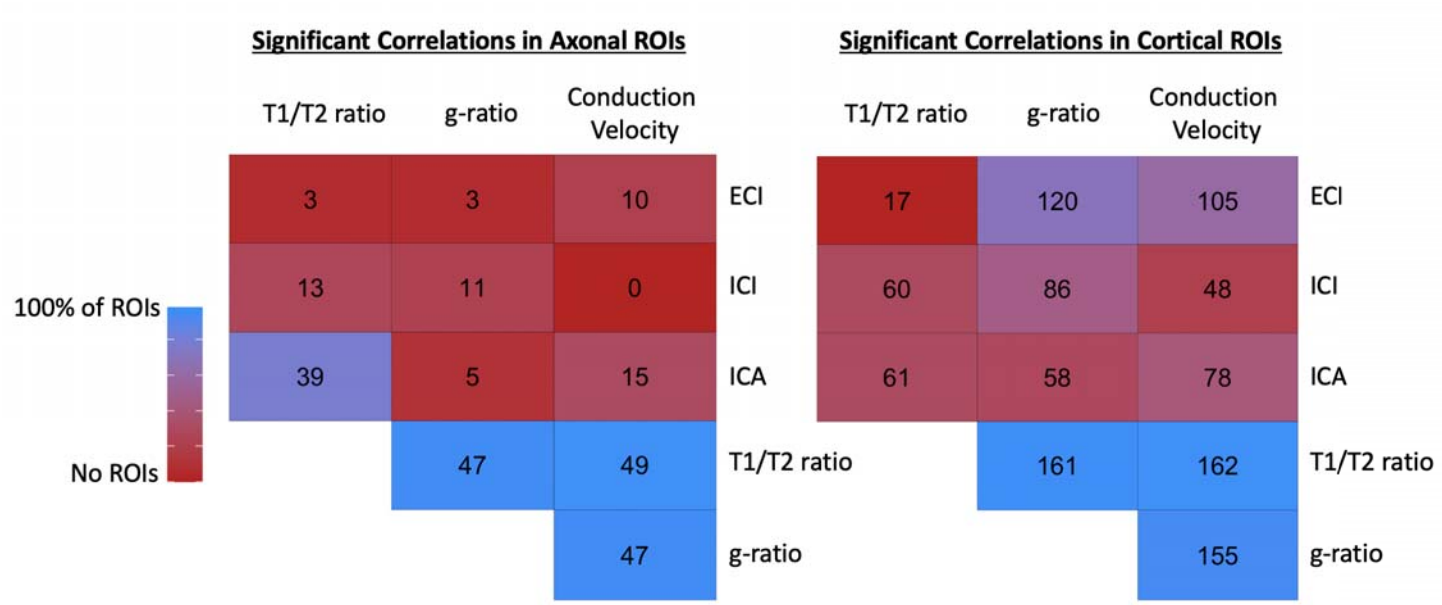

Figure 3: Matrix displaying number of ROIs across axonal areas and cortex that remained significantly associated within the same ROI with each of the different metrics used in this study. Metrics derived from T1/T2 ratio tended to have near universal significant associations between themselves (T1/T2 ratio, aggregate g-ratio, and aggregate conduction velocity). There was not very widespread associations in the axonal ROIs between metrics derived only from diffusion and metrics derived from T1/T2 ratio except for the ICA signal fraction (which is intended to measure intra-axonal signal fraction). ECI (extracellular water) signal fraction had negative associations while ICI and ICA had positive associations with T1/T2 ratio derived metrics. This was particularly true in the cortical ROIs where ECI signal fraction was significantly associated with aggregate g-ratio and aggregate conduction velocity in a majority of ROIs.

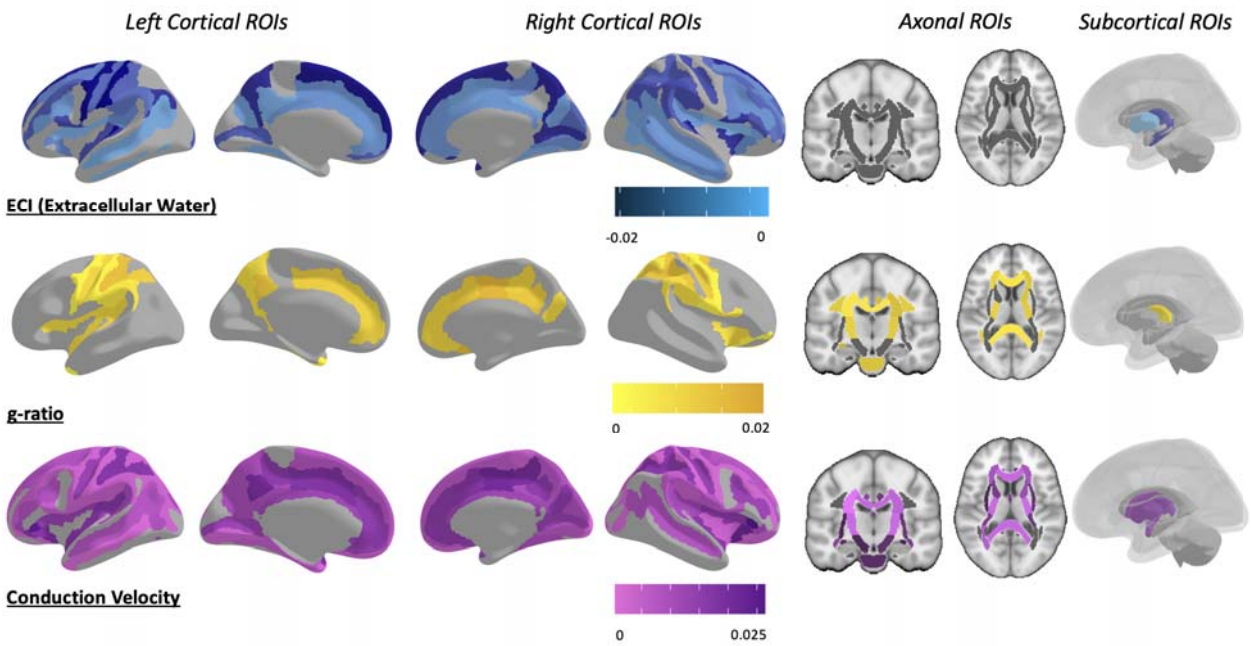

Figure 4: Map of ROIs that were significant at the p<0.05 level between ASD and TD after multiple comparison corrections. Colored by the slope of the relationship, with ASD individuals having greater extracellular water signal fraction, reduced aggregate g-ratio, and reduced aggregate conduction velocity in each of the significant ROIs. Aggregate conduction velocity was by far significantly different in more ROIs than any other metric, followed by the extracellular water compartment. However, there was a high degree of spatial specificity between the metrics, with aggregate g-ratio and aggregate conduction velocity involving extensive axonal areas and extracellular water differences primarily arising in the cortex and subcortex.

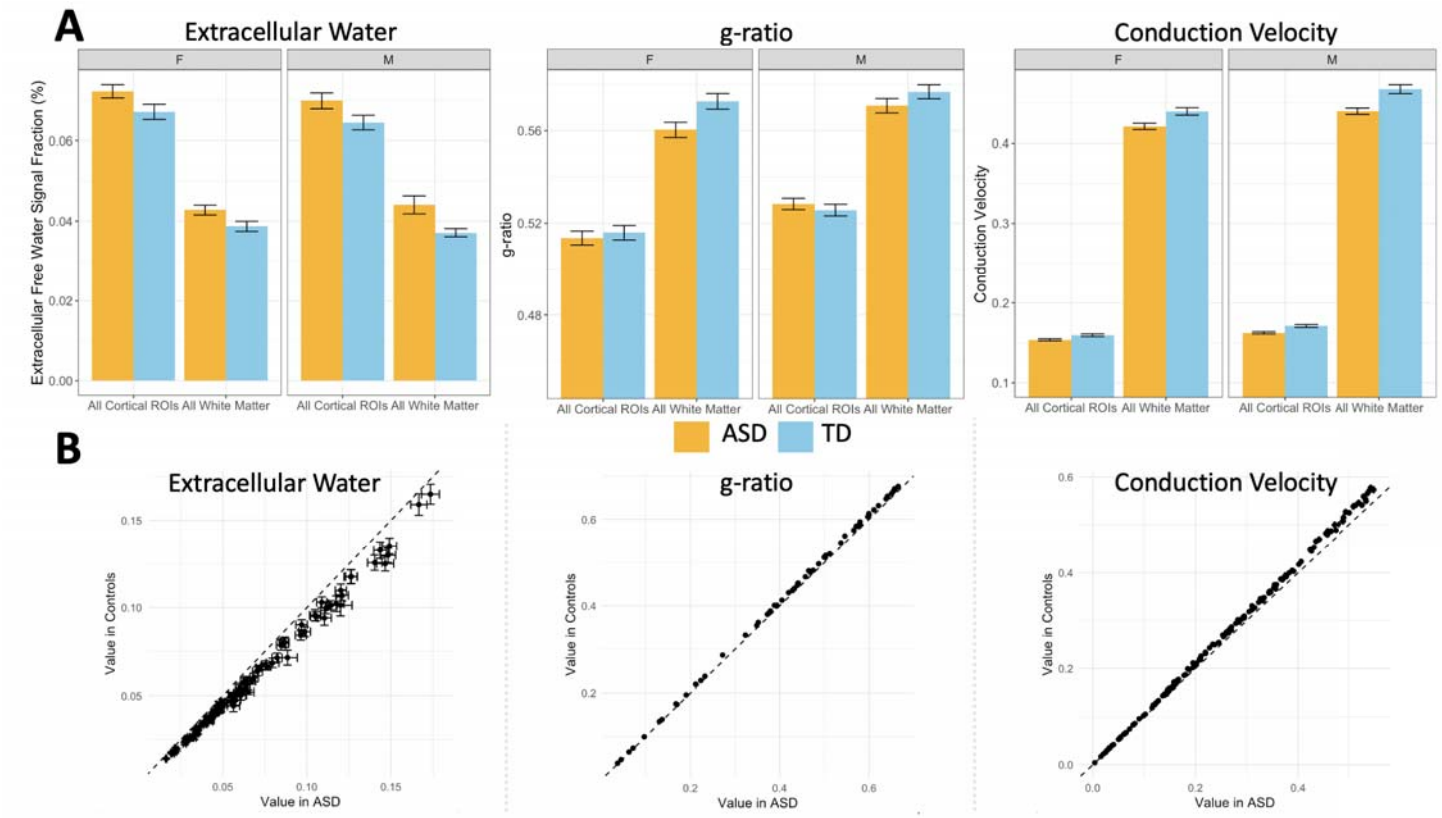

Figure 5: Chart displaying differences between extracellular free water, aggregate g-ratio, and aggregate conduction velocity levels in bilateral composite ROIs compared to TD participants, separated by sex. (A) Both boys and girls with ASD had significantly increased extracellular water, significantly decreased aggregate g-ratio, and significantly decreased conduction velocity. (B) Mean value in each significant ROI, after multiple comparison testing, with error bars representing standard error in each group. Dotted line represents x=y, showing that each individual ROI followed the directionality seen in the whole brain ROIs. Additionally, the effect appears to become more pronounced with higher mean value in extracellular value and aggregate conduction velocity.

Microstructural Metric	Anatomical Region	AUC
ECI (Extracellular Water)	All WM ROIs	0.8971
	All Cortical ROIs	0.7189
G-Ratio	All WM ROIs	0.7063
	All Cortical ROIs	0.4909
Conduction Velocity	All WM ROIs	0.7282
	All Cortical ROIs	0.7007

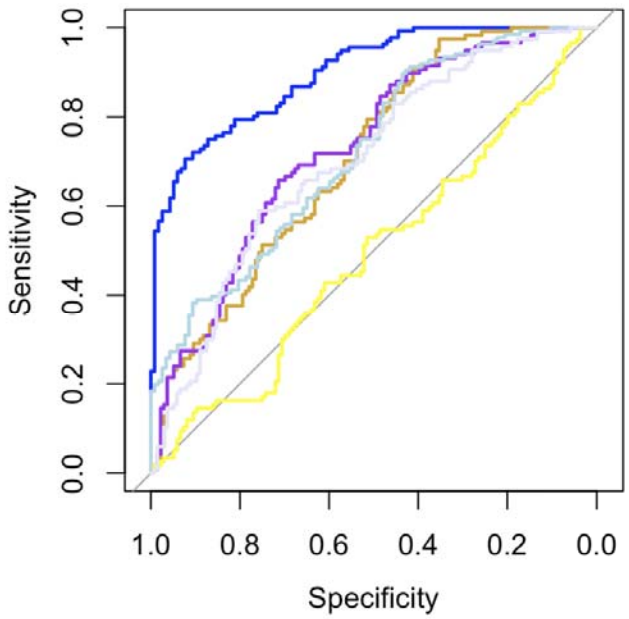

Figure 6: ROC analysis of the 3 microstructural metrics measured within the composite ROIs (axonal WM ROIs and Cortical ROIs, from the JHU WM atlas and Destrieux atlas) including AUC calculation. The same linear model as the ROI analysis was used to predict classification of subject diagnosis. Analysis indicated that ECI signal fraction within the composite WM ROI had the highest sensitivity and specificity to subject diagnosis, followed by aggregate conduction velocity within the composite WM ROI and ECI within the composite cortical ROI. Note that aggregate g-ratio had a sensitivity and specificity of approximately chance within the composite cortical ROI however this ROI was not statistically significant in the primary regional analysis.

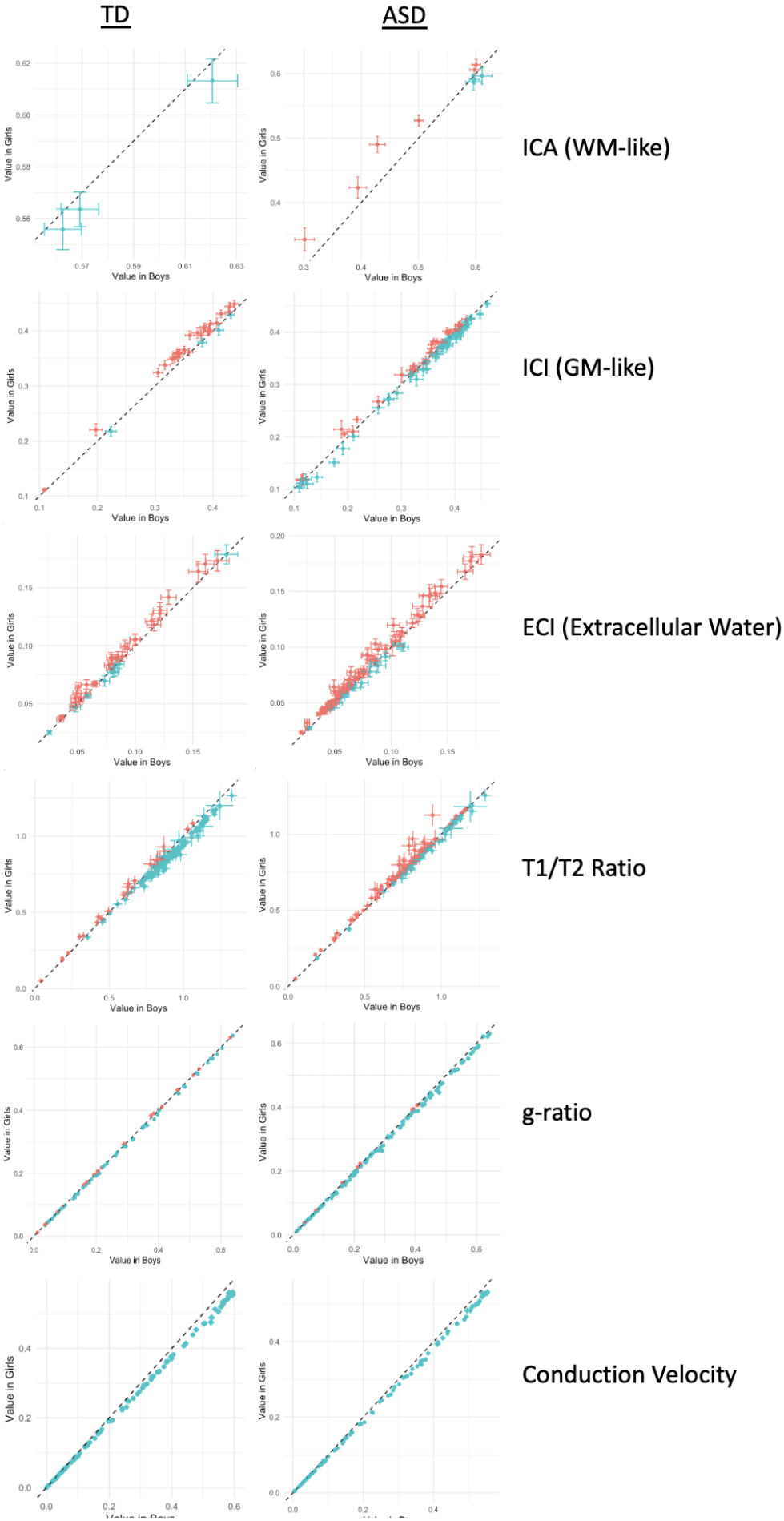
TD
ASD
ICA (WM-like)
ICI (GM-like)
ECI (Extracellular Water)
T1/T2 Ratio
g-ratio
Conduction Velocity
Value in Girls
Value in Boys

*Figure 7: Series of charts displaying mean microstructural values of ROIs significantly associated with age, colored by sex and separated between ASD and TD participants. Diagnosis groups show varying relationships with aging that are not consistent across sexes, with far higher T1/T2 ratio values in TD boys compared TD girls, while in ASD, girls tend to have higher T1/T2 ratio and ECI signal fraction values compared to boys. ASD boys meanwhile tend to have higher ICI (GM-like) signal fraction values, while in TD participants age-associated ROIs tend to have higher ICI (GM-like) values in girls. Aggregate conduction velocity and aggregate g-ratio do not seem to differ between ASD and TD in their age*sex interaction.*

Tables:

Microstructure Metric	Region	Diagnosis	Sex	Age	Intracranial Volume	IQ
ECI (Extracellular Water)	Total	93	0	94	2	0
	Subcortical GM	7	0	2	2	0
	Neocortex	84	0	91	0	0
	Axonal WM	0	0	0	0	0
ICI	Total	0	0	93	17	0
	Subcortical GM	0	0	2	3	0
	Neocortex	0	0	89	14	0
	Axonal WM	0	0	0	0	0
ICA	Total	0	0	36	12	0
	Subcortical GM	0	0	2	1	0
	Neocortex	0	0	33	11	0
	Axonal WM	0	0	0	0	0
T1/T2 Ratio	Total	0	0	200	128	0
	Subcortical GM	0	0	14	9	0
	Neocortex	0	0	138	86	0
	Axonal WM	0	0	46	31	0
Aggregate g-ratio	Total	61	0	144	17	1
	Subcortical GM	3	0	12	3	0
	Neocortex	38	0	111	7	0
	Axonal WM	19	0	20	7	1
Aggregate Conduction Velocity	Total	155	0	124	206	0
	Subcortical GM	11	0	3	14	0
	Neocortex	104	0	85	142	0
	Axonal WM	38	0	34	48	0

Table 1: Table summarizing the number of ROIs from each microstructural metric and each anatomical subgroup that were significant at the $p<0.05$ level for each variable after multiple comparison corrections. The total value for each includes the 2 additional composite ROIs. The right cerebral peduncle was the only aggregate g-ratio significantly related to IQ.